

1 Nonlinear increase in seawater $^{87}\text{Sr}/^{86}\text{Sr}$ in the Oligocene to 2 early Miocene and implications for climate-sensitive 3 weathering

4
5 Heather M. Stoll¹, Leopoldo D. Pena², Ivan Hernandez-Almeida¹, Jose Guitian^{1*}, Thomas
6 Tanner¹, Heiko Pälike³

7 ¹Department of Earth Science, ETH Zurich, Zurich, 8092 Switzerland

8 ²GRC Geociències Marines, Dept. Dinàmica de la Terra i de l'Oceà, Facultat de Ciències de la Terra, Universitat
9 de Barcelona, Barcelona, 28080 Spain

10 ³MARUM Centre for Marine Environmental Sciences, University of Bremen, Bremen, 28359 Germany
11

12 *Correspondence to:* Heather M. Stoll (heather.stoll@erdw.ethz.ch)

13 **Present address:* Centro de Investigación Mariña, Universidade de Vigo, GEOMA, Vigo, 36310, Spain

14 **Abstract.** The $^{87}\text{Sr}/^{86}\text{Sr}$ of marine carbonates provides a key constraint on the balance of continental weathering
15 and hydrothermal Sr fluxes to the ocean, and mid-Oligocene to mid-Miocene features the most rapid rates of
16 increase in the $^{87}\text{Sr}/^{86}\text{Sr}$ of the Cenozoic. Because previous records of the $^{87}\text{Sr}/^{86}\text{Sr}$ increase with time were based
17 on biostratigraphically defined age models in diverse locations, it was difficult to unambiguously distinguish m.y.
18 scale variations in the rate of $^{87}\text{Sr}/^{86}\text{Sr}$ change from variations in sedimentation rate. In this study, we produce
19 the first $^{87}\text{Sr}/^{86}\text{Sr}$ results from an Oligocene to early Miocene site with a precise age model derived orbital tuning
20 of high resolution benthic $\delta^{18}\text{O}$, at the Equatorial Pacific Ocean Drilling Program (ODP) Site 1218. Our new
21 dataset resolves transient decreases in $^{87}\text{Sr}/^{86}\text{Sr}$, as well as periods of relative stasis. These changes can be directly
22 compared with the high resolution benthic $\delta^{18}\text{O}$ in the same site. We find slowing of the rate of $^{87}\text{Sr}/^{86}\text{Sr}$ increase
23 coincides with the onset of Antarctic ice expansion at the beginning of the Mid-Oligocene Glacial Interval, and a
24 rapid steepening in the $^{87}\text{Sr}/^{86}\text{Sr}$ increase coincides with the benthic $\delta^{18}\text{O}$ evidence for rapid ice retreat. This pattern
25 may reflect either northward shifts in the Intertropical Convergence Zone precipitation to areas of nonradiogenic
26 bedrock, and/or lowered weathering fluxes from highly radiogenic glacial flours on Antarctic. We additionally
27 generate the first $^{87}\text{Sr}/^{86}\text{Sr}$ data from ODP Site 1168 [on the Tasman Rise](#) and Integrated Ocean Drilling Program
28 (IODP) Site 1406 [of the Newfoundland Margin](#) during the Oligocene to early Miocene to improve the precision
29 of age correlation of these Northern Hemisphere and Southern Hemisphere mid-latitude sites, and to better
30 estimate the duration of early Miocene hiatus and condensed sedimentation.
31

32 1 Introduction

33 The mid-Oligocene through the mid-Miocene features the fastest rate of change in seawater $^{87}\text{Sr}/^{86}\text{Sr}$ of
34 the Cenozoic, evidence of significant change in the balance of Sr sources to the ocean. Although the precise

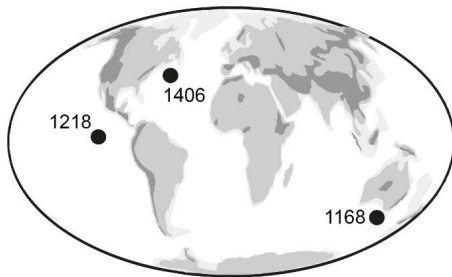
Formatted: Left: 2.54 cm, Right: 2.54 cm, Top: 2.54 cm,
Bottom: 2.54 cm, Width: 21 cm, Height: 29.7 cm, Header
distance from edge: 1.25 cm, Footer distance from edge:
1.25 cm, From text: 0 cm

35 causes of the Cenozoic $^{87}\text{Sr}/^{86}\text{Sr}$ change remain under discussion, to first order the rise reflects an increase in the
36 supply of dissolved Sr sourced from weathering of older rocks of higher $^{87}\text{Sr}/^{86}\text{Sr}$, which are found on continents,
37 compared to the supply of dissolved Sr from rocks of lower $^{87}\text{Sr}/^{86}\text{Sr}$ characterizing submarine volcanic
38 weathering and subaerial weathering of young volcanic provinces (Palmer and Elderfield, 1985). This change in
39 balance of sources can be accomplished by one or more processes including decrease in rate of hydrothermal
40 weathering, increase in total continental weathering, or changes in the $^{87}\text{Sr}/^{86}\text{Sr}$ of continental weathering flux due
41 to either changes in the location of most intense weathering or changes in the composition and average age
42 (Peucker-Ehrenbrink and Fiske, 2019) of rocks exposed to weathering.

43 The Oligocene-early Miocene is a period of very rapid increase in $^{87}\text{Sr}/^{86}\text{Sr}$, with multiple possible drivers
44 including the unroofing of highly radiogenic source rocks in the Himalaya (Galy et al., 1996; Yang et al., 2022;
45 Myrow et al., 2015). Within the Oligocene-early Miocene period of rapid increase in $^{87}\text{Sr}/^{86}\text{Sr}$, some previous
46 studies have suggested the potential for 1-3 million year timescale variations in the rate of increase (Oslick et al.,
47 1994) and proposed that the liberation of Sr from silicate weathering may respond to changes in the production
48 and exposure of glacially floured rock on Antarctica (Miller et al., 1991; Oslick et al., 1994; Zachos et al., 1999).
49 However, the precision of estimates of the rate of change in $^{87}\text{Sr}/^{86}\text{Sr}$ are limited by the precision of the
50 independent age model in marine records. Where age model control points are of low resolution or low certainty,
51 changes in sedimentation rate may cause apparent variations in the rate of change in $^{87}\text{Sr}/^{86}\text{Sr}$, so that changes in
52 the rate of $^{87}\text{Sr}/^{86}\text{Sr}$ cannot be confidently inferred. To date, available $^{87}\text{Sr}/^{86}\text{Sr}$ data for the Oligocene and early
53 Miocene is derived from deep sea sediment cores featuring only biostratigraphically derived age models, whose
54 precision is limited by the biostratigraphic sampling resolution as well as the potential for diachroneity among
55 events. Precision on such age models can be limited by long distances between examined biostratigraphic points
56 in the core and the potential for diachroneity in the first occurrence or last occurrence of taxa in diverse locations,
57 and may feature uncertainties from 0.5 to 4 m-million years. (Miller et al., 1988). Over the last decade,
58 astrochronology eyeleostratigraphy has emerged as a powerful independent chronometer, and the success of
59 continuous coring and splicing of deep ocean sediment cores has enabled the elaboration of precise independent
60 age models based on orbital tuning of high resolution benthic $\delta^{18}\text{O}$ records (Pälike et al., 2006; Liebrand et al.,
61 2016; Westerhold et al., 2020; De Vleeschouwer et al., 2017).

62 In this study, we seek to apply the independent orbitally tuned Oligocene chronology for two purposes.
63 First, we seek to evaluate the potential for dynamic changes in Sr sources by producing a $^{87}\text{Sr}/^{86}\text{Sr}$ (Westerhold et
64 al., 2020) record from a site with an independent orbitally-resolved age model, Ocean Drilling Program (ODP)
65 Site 1218 from the Equatorial Pacific (Figure 1), for which original chronology (Pälike et al., 2006) was recently
66 updated (Westerhold et al., 2020) (Pälike et al., 2006; Westerhold et al., 2020). The very rapid rate of change in
67 seawater $^{87}\text{Sr}/^{86}\text{Sr}$ also provides the opportunity for improved age correlation among distal sites (Mcarthur et al.,
68 2020). Therefore, our second objective is to improve the fidelity of the age model for two further sites which
69 currently lack an orbitally resolved age model, using existing reference curves and the Site 1218 record as an
70 additional reference. For this objective, we focus on North Atlantic International Ocean Discovery Program Site
71 1406 (Newfoundland Margin) and Southern Ocean ODP Site 1168 (Tasman Rise), both emerging as important
72 sites for Oligocene to early Miocene paleoceanographic studies (Scher et al., 2015; Hoem et al., 2022; Hoem et
73 al., 2021; Guitián and Stoll, 2021; Kim and Zhang, 2022; Egger et al., 2018; Liu et al., 2018; Spray et al., 2019;
74 Boyle et al., 2017). At site 1406, Sr isotope stratigraphy improves constraints on the duration of Site 1406 features

75 a hiatus of poorly constrained duration in the early Miocene hiatus (van Peer et al., 2017b; Norris et al., 2014).
76 The Oligocene to Early Miocene Southern Ocean paleogeography produced strong provincialism in many marine
77 taxa from Site 1168, so synchronicity with global biostratigraphic datums is uncertain. For paleoclimatic study,
78 tuning to Site 1218 offers the advantage of providing a precise link with the complete benthic $\delta^{18}\text{O}$ record and
79 therefore enabling direct correlation to the highest resolution paleoclimatic record available for this time interval.
80 **Figure 1. Location of ODP 1218, IODP 1406, and ODP 1168 with paleogeography during the Oligocene-Miocene**
81 **Transition. Reconstruction was made using the plate tectonic reconstruction service ODSN (www.odsn.de).**



2 Sites and Methods

2.1 Sediments

Ocean Drilling Program (ODP) Leg 199, Site 1218, equatorial Pacific ($8^{\circ}53.378'N$, $135^{\circ}22.00'W$, 4.8-km water depth) features a detailed astrochronologic age model from benthic $\delta^{18}\text{O}$ originally spanning 22 to 25 Ma (Pälike et al., 2006). Subsequently, continuous tuning at precision of the 100 ky eccentricity cycle from 21.81 Ma through the lowermost Oligocene was generated on the GTS-2020 CENOGRID timescale (Westerhold et al., 2020). In Site 1218 we sought high resolution in the Middle Oligocene Glacial Interval (MOGI), previously hypothesized to feature inflection points in the $^{87}\text{Sr}/^{86}\text{Sr}$ curve (Oslick et al., 1994). We targeted samples between 59.93 and 211.94 revised meter core depth (rmcd). Due to the modest carbonate content of Site 1218, not all targeted sample intervals contained sufficient foraminifera for analysis. We have picked >2 mg of mixed species of planktonic or mixed species of benthic foraminifera, depending on the abundance in each sample. From some samples, populations of both benthic and planktic forams could be procured and we report the averaged $^{87}\text{Sr}/^{86}\text{Sr}$ ratio for the two populations.

Integrated Ocean Drilling Program (IODP) Expedition 342 recovered Paleogene to Neogene sedimentary sequences in contourite drift deposits off the coast of Newfoundland in the Northwestern Atlantic. Here we focus on Site 1406 ($40^{\circ}21.0'N$, $51^{\circ}39.0'W$; 3814 mbsl) with samples dominantly from Hole A, but including a few samples from Holes B and C. The composite depth scale for the site (CCSF-A) is based on physical properties and trace element ratios from XRF Scanner (van Peer et al., 2017b) and is under revision as further benthic foraminifera and fine fraction stable isotope data are produced. Consequently, where exclusively data from Hole A are presented, we illustrate depth on CSF-A scale; where samples from all sites are plotted, we illustrate on the composite CCSF-A scale but where exclusively data from Hole A are presented, we illustrate depth on CSF-A scale as this latter scale will not be revised; both depth scales are provided in data tables. Based on available biostratigraphy and previous age models (Norris et al., 2014) (van Peer et al., 2017b), we sought samples spanning age range 17 to 30 Ma, represented by depths from 23.9 to 200 m on the CCSF-A depth scale. In the Southern Hemisphere, ODP Site 1168 was drilled offshore of the Australian plate at the western margin of Tasmania, at $43^{\circ}36.57'S$ and $139^{\circ}144'24.76'E$, and 2463m water depth. This sequence is within a graben-developed basin with sediment accumulation since the latest Eocene (Exon et al., 2004). Based on available biostratigraphy (Stickley et al., 2004), we selected samples from Hole A, spanning the 16 to 27 Ma interval,

114 representing sediments from 278 to 562 m depth ~~on the mbsf on the CSF-A~~ depth scale used for ODP sites of this
115 generation. Mixed planktonic foraminifera were picked for both sites 1406 and 1168.

116 2.2 Analytical

117 Strontium isotope ratios ($^{87}\text{Sr}/^{86}\text{Sr}$) were measured on ~2 mg of cleaned foraminifera carbonates.
118 Foraminifera samples were crushed open under binocular inspection and the fragments were rinsed several times
119 in MilliQ water, methanol and ultrasonicated to remove detrital contaminants (Pena et al., 2005). Each sample
120 was treated individually to ensure that sufficient rinsing steps were applied. Cleaned fragments were dissolved in
121 dilute double distilled nitric acid, and the resulting solution centrifuged at medium speed for 20 minutes to remove
122 any potential detrital material left in the samples. The supernatant was transferred to clean Savillex-PFA beakers
123 and Sr was chemically separated from sample matrix and interfering Rb using Triskem Sr-Spec resin through
124 column chromatography procedures at the LIRA ultra-clean laboratory (Universitat de Barcelona).

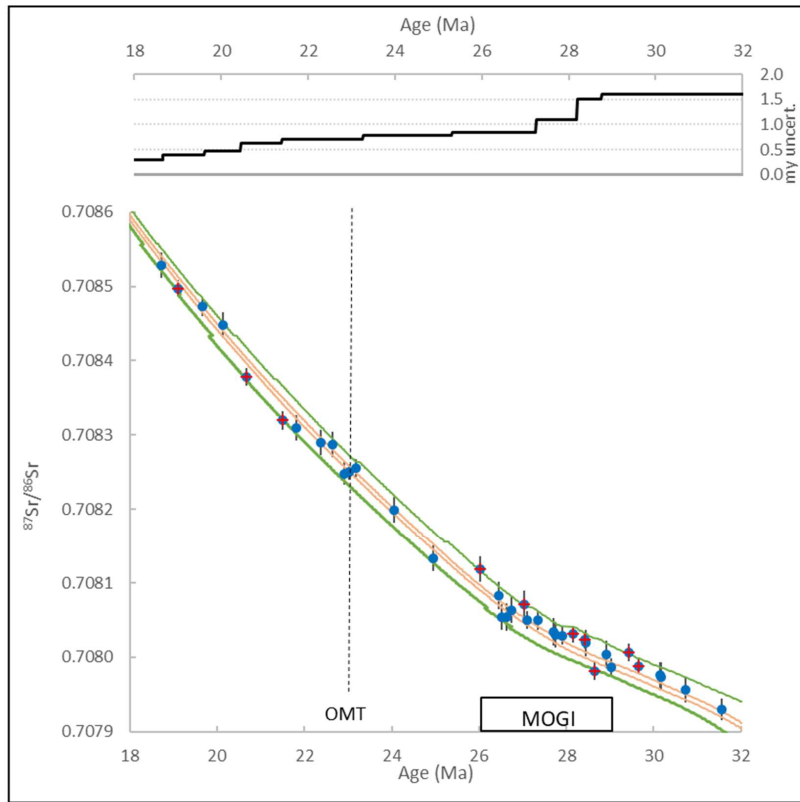
125 Following sample purification, Sr isotope ratios were determined by multicollector inductively coupled
126 mass spectrometry on a Nu Instruments (Wrexham, UK) Plasma 3 MC-ICPMS at the University of Barcelona
127 (CciT-UB). For the determination of the $^{87}\text{Sr}/^{86}\text{Sr}$ isotope ratios, the contribution of ^{87}Rb to the ^{87}Sr signal was
128 corrected from the measurement of the ^{85}Rb signal, assuming a $^{87}\text{Sr}/^{85}\text{Sr}$ ratio of 0.38562. The ^{86}Kr interference
129 on ^{86}Sr , caused by impurities in the argon gas, was also corrected by measuring the ^{83}Kr signal, and assuming a
130 $^{83}\text{Kr}/^{86}\text{Kr}$ value of 0.66453. $^{87}\text{Sr}/^{86}\text{Sr}$ ratios were normalized for instrumental mass bias to $^{86}\text{Sr}/^{88}\text{Sr} = 0.1194$.
131 Instrumental drift was corrected by sample-standard bracketing (SSB) using NBS987 = 0.710249 as the primary
132 standard with matching standard and sample Sr concentrations. External analytical reproducibility during the
133 session was ± 0.000018 (2σ , $n=19$). Procedural blanks are routinely measured at every analytical session. Typical
134 procedural Sr blanks (including sample cleaning, purification and analysis) are 369 ± 264 pg, $n=12$, 1 σ SD.
135 Blanks are systematically corrected for every measurement and the effect of the correction is in the sixth decimal
136 place of the $^{87}\text{Sr}/^{86}\text{Sr}$ ratios, well below the external reproducibility of the analytical method (5th decimal place).
137 Values are normalized to SRM 987 using $^{86}\text{Sr}/^{86}\text{Sr}$ of 0.1194 and $^{87}\text{Sr}/^{86}\text{Sr}$ of 0.710249. This is identical to the
138 normalization of (Mcarthur et al., 2020) using $^{87}\text{Sr}/^{86}\text{Sr}$ 0.709174 for modern marine-Sr (EN-1 and similar),
139 equivalent to 0.710248 for SRM(NIST) 987.

140 3 Results

141 Our new data from Site 1218 on the Cenogrid age model (Figure 21, Table 1), reveal a similar long term
142 amplitude and rate of rise in $^{87}\text{Sr}/^{86}\text{Sr}$ as previously reported data on biostratigraphically constrained age models
143 (Mcarthur et al., 2020). However, the new data reveal a 1 m.y. duration period of negligible $^{87}\text{Sr}/^{86}\text{Sr}$ rise (27-28
144 Ma) and local reversals in the overall trend of increasing $^{87}\text{Sr}/^{86}\text{Sr}$ during the Middle Oligocene Glacial Interval
145 (MOGI) and at the Oligo-Miocene transition. The new data also reveal several intervals of especially abrupt
146 increase in $^{87}\text{Sr}/^{86}\text{Sr}$ within and at the end of the MOGI.

Formatted: Superscript

Formatted: Superscript



149

150 **Figure 12:** $^{87}\text{Sr}/^{86}\text{Sr}$ results from Site 1218 (blue circles with 2σ analytical uncertainty shown). The orange lines show
 151 the upper and lower bounds of the LOESS fit of biostratigraphically defined $^{87}\text{Sr}/^{86}\text{Sr}$ (Mcarthur et al., 2020). Samples
 152 falling outside the biostratigraphically defined long term curve are highlighted in red. The green lines illustrate
 153 expanded age bounds for LOESS fit of biostratigraphically constrained age models (Mcarthur et al., 2020). Upper
 154 panel illustrates the width of the age uncertainty of the expanded bounds. The Middle Oligocene Glacial Interval
 155 (MOGI) from 29 to 26 Ma is labelled, as is the Oligocene-Miocene Transition (OMT). **We highlight this duration of**
 156 **MOGI on the basis of the 1218 benthic $\delta^{18}\text{O}$ record as indicated in Figure 4; it is slightly longer than the 28 to 26.3 Ma**
 157 **MOGI defined by** (Liebrand et al., 2016; Liebrand et al., 2017)

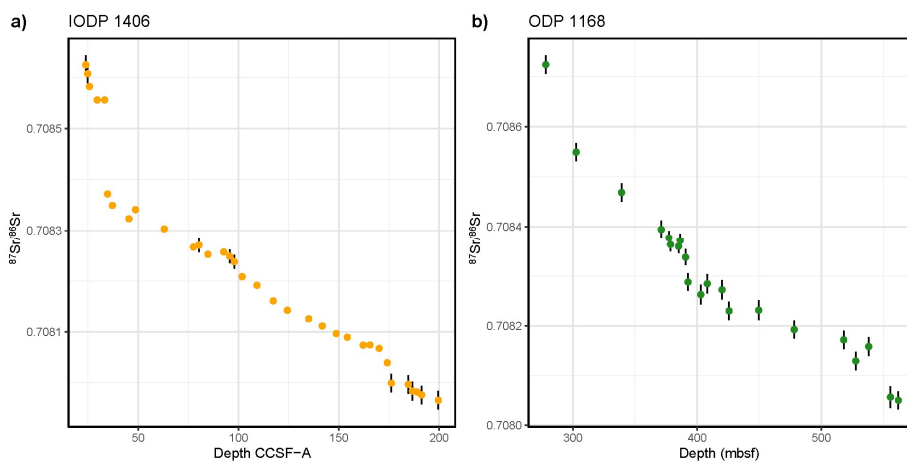
Formatted: Font: Symbol

Formatted: Superscript

158

159 In Site U1406, a prominent reversal in the $^{87}\text{Sr}/^{86}\text{Sr}$ rise is observed between 48.7 and 45.4 m (Figure
 160 32a, depths described on the CCSF-A scale). A significant jump in $^{87}\text{Sr}/^{86}\text{Sr}$ suggests an appreciable hiatus
 161 between 33.3 m and 34.7 m. The abrupt change in $^{87}\text{Sr}/^{86}\text{Sr}$ between 176.2 and 170.1 may also indicate a hiatus
 162 or significantly condensed interval. In Site 1168 (Figure 32b), a prominent reversal in the $^{87}\text{Sr}/^{86}\text{Sr}$ rise occurs
 163 between 538.2 and 527.8 m CSF-A.

164



165

166 **Figure 23:** $^{87}\text{Sr}/^{86}\text{Sr}$ results from a) U1406 and b) 1168. Vertical error bars indicate 2σ analytical uncertainty where it
 167 exceeds the size of the plotted symbol.

168 **4 Discussion**

169 **4.1 Variation in the rate of change of $^{87}\text{Sr}/^{86}\text{Sr}$ in Site 1218**

170

171 The steep long term Oligocene to early Miocene increase in $^{87}\text{Sr}/^{86}\text{Sr}$ is long recognized and variably
 172 attributed to exhumation of readily weathered radiogenic bedrock during the Himalayan orogeny (Krishnaswami
 173 et al., 1992; Raymo et al., 1988), or to accelerated weathering of radiogenic bedrock in Antarctica with the onset
 174 of its glaciation (Miller et al., 1991). The cause of this long term increase is beyond the scope of this study and
 175 our focus is on the variability in the rate of increase within the Oligocene to early Miocene.

176 Significantly, the precise independent chronology of Site 1218 confirms that the long term Oligocene
 177 and early Miocene increase in $^{87}\text{Sr}/^{86}\text{Sr}$ is punctuated by significant structure, including reversals, periods of
 178 negligible $^{87}\text{Sr}/^{86}\text{Sr}$ increase, as well as more abrupt increases in $^{87}\text{Sr}/^{86}\text{Sr}$. Reversals beyond analytical
 179 uncertainty are also seen in published high resolution Mid-Oligocene $^{87}\text{Sr}/^{86}\text{Sr}$ records from both ODP Site 522
 180 (Reilly et al., 2002) and ODP Site 689B (Mead and Hodell, 1995), suggesting that they are a robust feature of the
 181 Oligocene ocean Sr cycle. The uncertainty in absolute chronology complicates the inference of m.y. scale periods
 182 of stasis or abrupt $^{87}\text{Sr}/^{86}\text{Sr}$ increase in previously published records with biostratigraphic age models. To further
 183 evaluate how the rate of change of $^{87}\text{Sr}/^{86}\text{Sr}$ deviates from a monotonic increase from 32 to 18 Ma, we generate
 184 a smoothed fit to the data based on local linear regression model (Figure 43). In the model, local regressions were
 185 based on 3 to 6 consecutive samples and age range of at least 0.25 Ma, with the exception of a single shorter span
 186 of only 0.18 Ma at 26 Ma. To estimate the rate of change, we illustrate the derivative of this smoothed fit, as well
 187 as the slope and its uncertainty for each linear segment (Figure 43b). This analysis illustrates periods of both
 188 more rapid increase as well as slowed or inverted $^{87}\text{Sr}/^{86}\text{Sr}$ increase or a decrease.

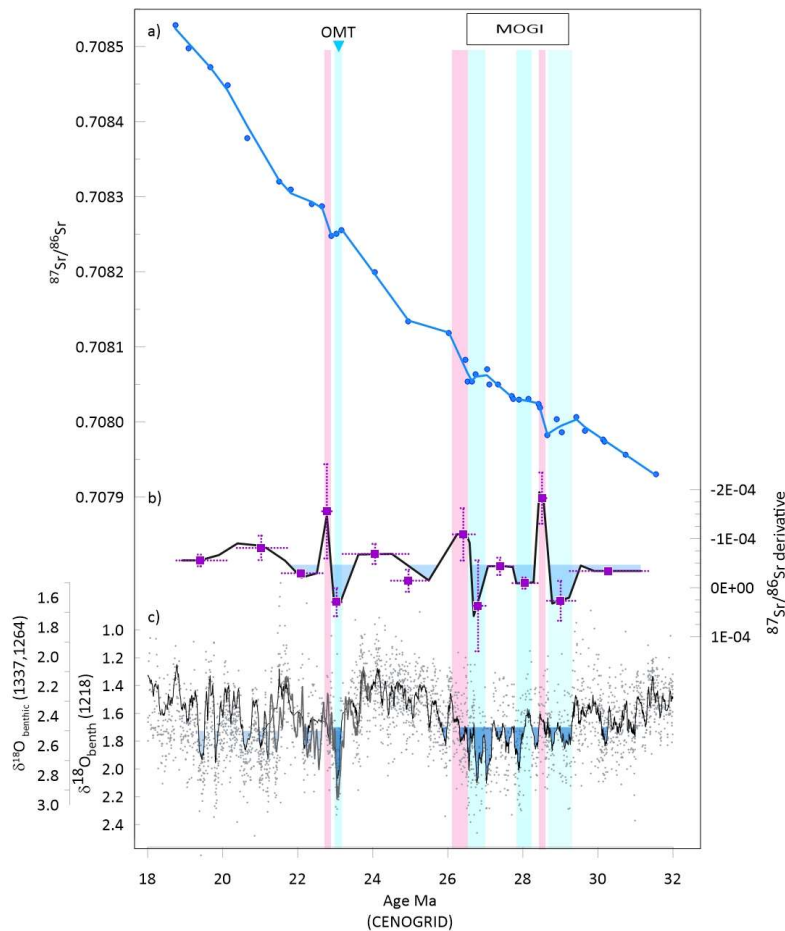
189 In Site 1218, appreciably lower rates of $^{87}\text{Sr}/^{86}\text{Sr}$ increase (or even $^{87}\text{Sr}/^{86}\text{Sr}$ decrease) occur centered at
 190 29 Ma and 26.8 Ma during the MOGI, and at 23 Ma during the OMT (Figure 43). Each of these periods is

191 followed by a large acceleration of $^{87}\text{Sr}/^{86}\text{Sr}$ increase. Our new data provide the most precise comparison between
192 $^{87}\text{Sr}/^{86}\text{Sr}$ and the benthic $\delta^{18}\text{O}$ record of deep sea temperature and ice volume because the records derive from the
193 same deep sea sediment archive (without correlation uncertainty) and the benthic $\delta^{18}\text{O}$ record is very high
194 resolution, without aliasing which can occur in records sampled at resolution comparable or greater than periods
195 of orbital variation. The earliest slowing/reduction in the rate of $^{87}\text{Sr}/^{86}\text{Sr}$ increase and even decrease in $^{87}\text{Sr}/^{86}\text{Sr}$
196 which we resolve (centered at 29 Ma) coincides with the onset of heavier average benthic $\delta^{18}\text{O}$ demarcating the
197 Mid-Oligocene Glacial interval (MOGI), and the recovery of rapid $^{87}\text{Sr}/^{86}\text{Sr}$ increase coincides with a shift towards
198 more negative benthic $\delta^{18}\text{O}$ (ice volume decrease and/ or deep sea warming). The return to more intense glaciation
199 from 28 to 26.8 Ma yields a decrease in pronounced slowing of the rates of $^{87}\text{Sr}/^{86}\text{Sr}$ increase. The subsequent
200 acceleration of $^{87}\text{Sr}/^{86}\text{Sr}$ increase at 26.5 Ma coincides with the onset of the negative shift in benthic $\delta^{18}\text{O}$ marking
201 the end of the MOGI with ice volume decrease and/ or deep sea warming. The reduction of $^{87}\text{Sr}/^{86}\text{Sr}$ increase (or
202 $^{87}\text{Sr}/^{86}\text{Sr}$ decrease) at the OMT coincides with an intense glacial phase, and subsequently a consequent acceleration
203 of $^{87}\text{Sr}/^{86}\text{Sr}$ increase at the end of the glacial phase. This event may coincide with the post-OMT acceleration
204 previously defined as 22.4 Ma on the Cande and Kent (Cande and Kent, 1992) timescale (Oslick et al., 1994).
205 We are unable to evaluate if there are similar <0.5 Ma variations in the rate of $^{87}\text{Sr}/^{86}\text{Sr}$ change between 26 and
206 23 Ma as our sample resolution is not high enough in this interval. The main changes in slope are significant at
207 the 68% CI (1s) level, but an increase in the sample resolution and number of data points would be needed to
208 confidently distinguish many of these differences at the 95% CI (2s) level.

209 Variations in the isotopic composition of Sr inputs on timescales of 10^5 yr are not expected to reflect
210 changes in ocean crustal production rate and hydrothermal flux, nor significant changes in the composition of
211 bedrock exposed on continents. Therefore, such changes are suggestive of change in either the intensity of
212 continental weathering relative to hydrothermal sources or changes in the locus of most intense continental
213 weathering among continental sources of contrasting $^{87}\text{Sr}/^{86}\text{Sr}$. For example, a short term relative increase in
214 weathering intensity in areas underlain by younger average bedrock compared to older average bedrock would
215 lead to a decreased $^{87}\text{Sr}/^{86}\text{Sr}$ of the riverine Sr flux and the marine reservoir. Alternatively, a short term decrease
216 in the intensity of weathering and thereby in the continental Sr flux (higher $^{87}\text{Sr}/^{86}\text{Sr}$ than the hydrothermal flux)
217 could also lead to a decreased marine $^{87}\text{Sr}/^{86}\text{Sr}$. In either case, the long residence time of Sr in the ocean would
218 result in lags between onset of elevated fluxes and peak response in ocean chemistry and would cause significant
219 attenuation of the time-varying input signal. An example of the phasing and amplitude variation in the $^{87}\text{Sr}/^{86}\text{Sr}$
220 of the Sr influx which could yield the observed trends in marine $^{87}\text{Sr}/^{86}\text{Sr}$ is illustrated in Supplementary Figure
221 1. for a sample residence time of 2.5 million years as suggested by (Hodell et al., 1990) Hodell et al., 1990. A
222 shorter residence time has been proposed for the Oligocene by (Paytan et al., 2021); for a shorter residence time,
223 a less extreme forcing would be required to simulate our observations. We caution that because the Sr isotopic
224 system of the Oligocene to Early Miocene is underconstrained, the observations of oceanic $^{87}\text{Sr}/^{86}\text{Sr}$ do not provide
225 a unique solution for the variation in fluxes and/or their isotopic composition.

226

- Formatted: Not Highlight
- Formatted: Font: Not Bold, Font color: Auto
- Formatted: Font color: Auto
- Formatted: Font: Not Bold, Font color: Auto
- Formatted: Font color: Auto
- Formatted: Font: Not Bold, Font color: Auto
- Formatted: Font color: Auto
- Formatted: Font: Not Bold, Font color: Auto
- Formatted: Font color: Auto



227
 228 **Figure 43.** a) Measured Site 1218 $^{87}\text{Sr}/^{86}\text{Sr}$ (symbols) and the smoothed fit from local linear regression (blue line). b)
 229 the derivative of the smoothed fit (black line) and the slope of each linear segment (purple square), together with
 230 the uncertainty on the slope (vertical error bar, 68% confidence interval) and the age range of the local linear fit (horizontal bar).
 231 Shading indicates sectors in which $^{87}\text{Sr}/^{86}\text{Sr}$ rises more slowly than the average rate over 32 to 18 Ma. c) Benthic $\delta^{18}\text{O}$
 232 measurements (gray points) and lines showing 20 point running mean. From Site 1218 (black line from 21.46 to 32 Ma)
 233 (Pälike et al., 2006) and from the Cenozoic reference splice derived from U1337 (Holbourn et al., 2015) and ODP Site
 234 1264 (Westerhold et al., 2020) both scaled as in (Westerhold et al., 2020), as gray line from 21.2 to 24 Ma when
 235 overlapping with 1219 record, and black line from 18 to 21.2 Ma. All data are plotted on the orbitally tuned
 236 CENOGRID timescale (Westerhold et al., 2020). Blue shading highlights intervals with benthic $\delta^{18}\text{O}$ more positive
 237 than 1.7 ‰ in Site 1218 and 2.5 ‰ in Cenozoic reference splice 1264 and U1337. The Middle Oligocene Glacial Interval
 238 (MOGI) from 29 to 26 Ma is labelled, as is the Oligocene-Miocene Transition (OMT). Vertical blue and pink lines
 239 highlight intervals of slower and more rapid rate of change in $^{87}\text{Sr}/^{86}\text{Sr}$, respectively.

240 The coincidence of periods of slowed $^{87}\text{Sr}/^{86}\text{Sr}$ and the onset of glacial advance on Antarctica evidenced
 241 in benthic $\delta^{18}\text{O}$ suggests a climate control on the variations in the continental Sr flux on 10^5 yr timescales from
 242 one or both of these mechanisms. Changes in the location of intense rainfall, such as shift in the polar front or
 243 Intertropical Convergence Zone (ITCZ), could alter the locus of most intense weathering. Potentially, episodes
 244 of Antarctic glacial expansion could cause an equatorward movement of the SH westerlies and associated rainfall
 245 band, or could cause a mean ITCZ shift toward the northern Hemisphere. However, climatically-driven changes

246 in the position of main heavy rainfall belts such as ITCZ is usually limited to < 10 degrees latitude and may be
247 longitudinally variable (Atwood et al., 2020). A movement of precipitation belts would have a significant
248 consequence on global riverine $^{87}\text{Sr}/^{86}\text{Sr}$ only in cases of fortuitous distribution of bedrock of widely different
249 ages ~~across the length scale of ITCZ movement. -on similar~~ If a northward shift of the mean ITCZ significantly
250 increased the Sr flux from ~~at this~~ region of nonradiogenic Sr, the marine $^{87}\text{Sr}/^{86}\text{Sr}$ could experience a transient
251 ~~decrease-length-scale-as-movement-of-rainfall~~. One potential such configuration could be the exposure of highly
252 weatherable nonradiogenic rocks of the Deccan volcanic series of India and the Ethiopian Traps, located just north
253 of the equator in the late Oligocene (Kent and Muttoni, 2013).

254 It has also been proposed that glaciation can affect the weatherability of bedrock. Generally, highest riverine
255 dissolved Sr fluxes are produced from reactive young volcanic rock, as well as soluble carbonates, but the
256 mechanical flouring of less reactive rock types by glacial erosion can significantly increase their weatherability
257 and Sr contribution to the ocean. It has been suggested that weathering intensity of the Antarctic craton may have
258 evolved over the late Eocene through Oligocene, as glacial flouring of Antarctic bedrock increased the
259 weatherability of this continental Sr source (Miller et al., 1991; Oslick et al., 1994), contributing to the rise in
260 ocean $^{87}\text{Sr}/^{86}\text{Sr}$. Intermittent glaciation, characterized by significant changes in the spatial extent of ice coverage,
261 may alternately generate highly weatherable fine grained silicates in a subglacial weathering-limited environment
262 (low continental Sr fluxes) and then expose them to subaerial conditions of enhanced chemical weathering (high
263 continental Sr flux). On previous biostratigraphic age models, apparent accelerations in the rate of $^{87}\text{Sr}/^{86}\text{Sr}$
264 increase at 32, 28, 22.4, 19.5, and 16.5 Ma (on the Cande and Kent timescale) occur 1 m.y after deglaciation
265 midpoint inferred from benthic $\delta^{18}\text{O}$ maxima in ODP 747 (Oslick et al., 1994). This was interpreted to result from
266 the deglacial exposure which may have contributed to a transient increase in flux of radiogenic Sr to the ocean.

267 With higher resolution benthic $\delta^{18}\text{O}$ from 1218, we resolve more rapid responses of the $^{87}\text{Sr}/^{86}\text{Sr}$ ratio to several
268 deglaciation phases.

269 East Antarctica is inferred to be underlain dominantly by Proterozoic and Archean bedrock (Kirkham et
270 al., 1995). Exposed bedrock in East Antarctica is dominated by Archean and Proterozoic metamorphic rocks,
271 with Paleozoic igneous and sedimentary rocks additionally exposed in the Transantarctic mountains (Licht
272 and Hemming, 2017). Although the Sr isotopic composition of bedrock in Antarctica can be measured directly only
273 in current exposures in the Transantarctic mountains and coastal areas, crustal rocks at the perimeters of major ice
274 sheets may represent a major source of the sediment arriving at the margin and therefore weatherable during
275 retreat (Farmer et al., 2003). Because erosion rates are highest at the perimeter of Antarctic ice sheet (Jamieson
276 et al., 2010), the mapped bedrock in coastal areas may provide a reasonable representation of the source of
277 sediment arriving to the glacial margin and weatherable during retreat. Additionally, the fine grained component
278 of LGM tills exposed in the Ross Sea embayment provide constraints on modern underlying composition of
279 present erosion (Farmer et al., 2006). Present till composition includes very radiogenic compositions up to 0.740
280 attributed to erosion of the Neoproterozoic Beardsmore Formation, and compositions in the range of 0.720 to
281 0.735 typical of 500 Ma Granite Harbor Intrusive rocks exposed in southern part of Transantarctic Mountains and
282 the Wilson terrane Proterozoic gneisses (Farmer et al., 2006). However, a caveat is that the currently exposed
283 bedrock may be older than that exposed in the Oligocene due to denudation, and younger, less radiogenic bedrocks
284 may have contributed more to glacial flouring in the Oligocene, making global fluxes less sensitive to the Antarctic
285 weathering regime.

286 **4.2 Sr isotope constraints on age models of Site U1406 and Site 1168**

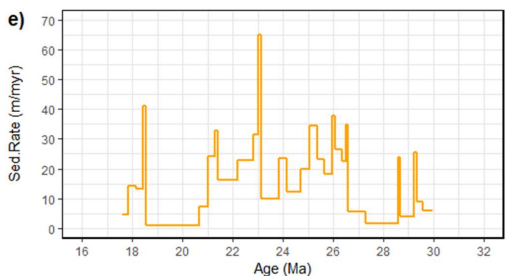
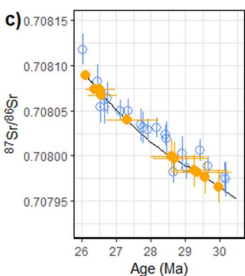
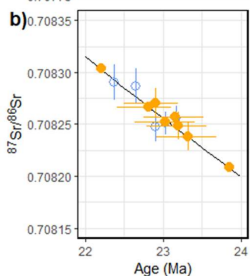
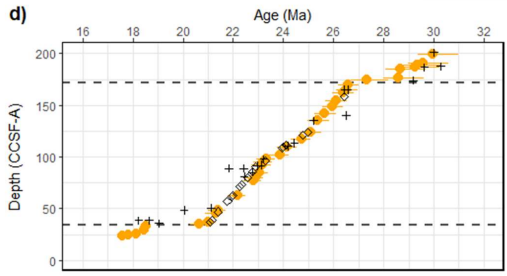
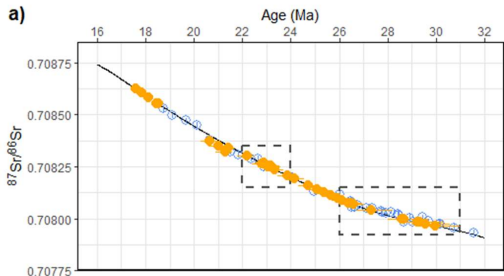
287 Previous approaches for Sr isotope stratigraphy for the Cenozoic have inferred a continuous rise in
288 $^{87}\text{Sr}/^{86}\text{Sr}$. The data from Site 1218 suggest several intervals with a negligible rate of rise and/or reversals. In the
289 interval from 28 to 30 Ma, 5 of our 9 samples feature $^{87}\text{Sr}/^{86}\text{Sr}$ ratios whose analytical 95% CI fall outside of the
290 bounds of the reference $^{87}\text{Sr}/^{86}\text{Sr}$ curve of that age generated from biostratigraphically constrained age models
291 (McArthur et al., 2020). For these intervals, particularly during the MOGI, age assignments from Sr isotope
292 stratigraphy have a higher uncertainty than previously inferred. In the interval from 28 to 30 Ma, the deviation
293 between the CENOGRID age and the reference curve ranges from 1.1 Ma older than the reference curve to 0.7
294 Ma younger, a significantly wider uncertainty than the +/- 120 to 180 ky uncertainty predicted for the reference
295 curve. In the early Miocene, between 21.7 and 19.4 Ma, a number of our Site 1218 CENOGRID ages also deviate
296 from the ages from the reference curve, by 0.18 to 0.42 Ma younger, a greater uncertainty than the +/- 70 to 50 ky
297 reported for the reference curve. Consequently, in deriving ages for Site U1406 and Site 1168 on the CENOGRID
298 scale from $^{87}\text{Sr}/^{86}\text{Sr}$, we expand the bounds of the age uncertainties from (McArthur et al., 2020) to encompass
299 the Site 1218 data (Figure 24, green bounds). The width of the resulting age uncertainty therefore ranges from
300 300 ky in the early Miocene to 1.6 My in the early-mid Oligocene.

301 In addition to these greater uncertainties, stratigraphic constraints prohibit reversals in ages where there
302 is no independent evidence for reworking or sediment disturbance. Our Site 1218 data indicate that reversals in
303 $^{87}\text{Sr}/^{86}\text{Sr}$ are certain within the time interval of 29-26 Ma, and likely at the OMT. Thus, in estimating ages for
304 1168 and U1406 based on $^{87}\text{Sr}/^{86}\text{Sr}$, we assign an initial age based on (McArthur et al 2020) but adjust the age to
305 preserve stratigraphic relationships (eg no age reversals in our age assignments). The detailed age models are
306 shown in Tables 2 and Table 3.

307 **4.2.1. Site U1406**

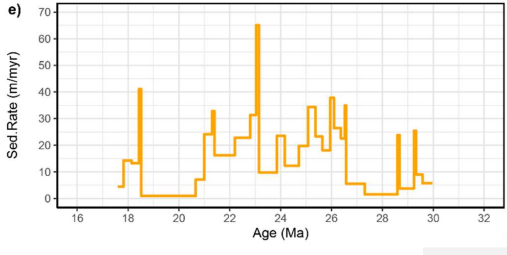
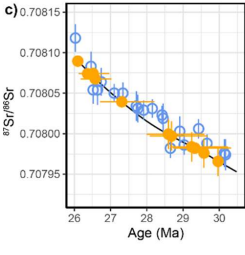
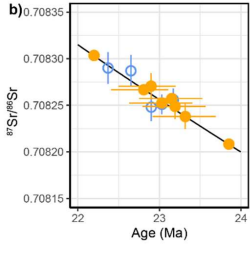
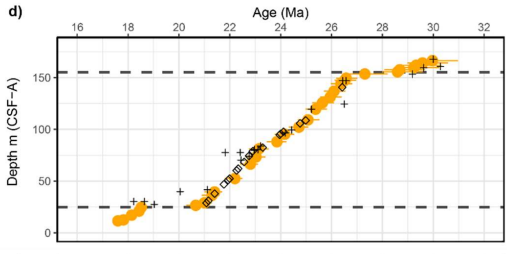
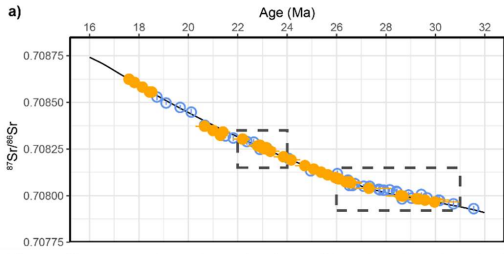
308 A condensed interval and hiatus have been recognized in the Oligocene to early Miocene sediments of
309 U1406 on the basis of bio- and magnetostratigraphy (Figure 5) (Norris et al., 2014; van Peer et al., 2017a).
310 Because of the slow rate of the Site U1406 $^{87}\text{Sr}/^{86}\text{Sr}$ change and reversals during the MOGI, the U1406 $^{87}\text{Sr}/^{86}\text{Sr}$
311 cannot precisely pinpoint the duration of the hiatus or condensed interval between 153 and 149 m (CSF-A) (Figure
312 54). The condensed interval could contain 2 m.y. (28.45 to 26.58 Ma) or < 1 m.y. (27.3 to 26.58). On the other
313 hand, the early Miocene condensed interval between 27 and 25 m (CSF-A) is constrained to represent 2 m.y.
314 Sustained high sedimentation rates are confirmed between 21 and 26 Ma. Between 26.4 and 21 Ma, the $^{87}\text{Sr}/^{86}\text{Sr}$
315 age model is in close agreement with that devised from magnetostratigraphy (Van Peer et al., 2017a). The Site
316 1406 $^{87}\text{Sr}/^{86}\text{Sr}$ data indicate that the uppermost 25 m of sediment in U1406, difficult to date due to sparse
317 biostratigraphic markers, was likely deposited between 18.5 and 17.6 Ma. Sustained high sedimentation rates
318 are confirmed between 21 and 26 Ma.

319
320



321

322



323

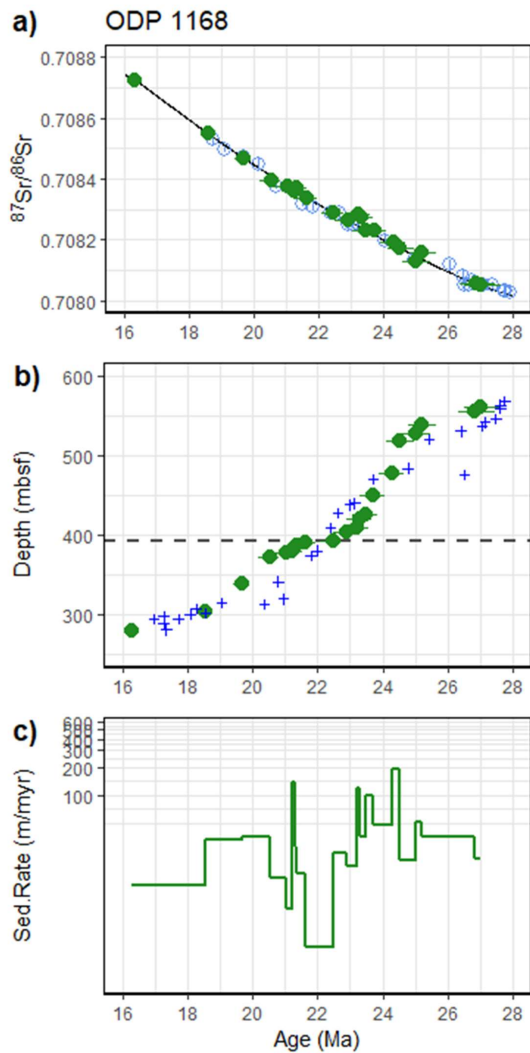


Figure 54. a) Site U1406 $^{87}\text{Sr}/^{86}\text{Sr}$ data (orange) vs age (CENOGRID scale) assigned here; also shown are the Site 1218 new data (blue) and the GTS LOESS curve (Mearthur et al., 2020). b. and c. show insets. For Site U1406, horizontal lines indicate the uncertainty in the age assignments. d) Age depth plot for U1406A on the CSF-A scale. Orange circles denote the ages from $^{87}\text{Sr}/^{86}\text{Sr}$ compared to previous biostratigraphy tiepoints (crosses; (Norris et al., 2014)) and magnetostratigraphy (open diamonds) (van Peer et al., 2017a). Horizontal dashed lines delimit the strongly condensed intervals; e) the inferred sedimentation rate.

4.2.2. Site 1168

This first $^{87}\text{Sr}/^{86}\text{Sr}$ stratigraphy for Site 1168 implies significant differences in inferred ages compared to existing biostratigraphy, including significantly higher sedimentation rates in the early Miocene (20.5 to 18.5 Ma), but comparably slower sedimentation rates between 21.6 and 22.5 Ma just after the OMT (Figure 56). This is slightly earlier than the early Miocene hiatus found in many deep sea sedimentary records between 19 to 20 Ma; however, in other deep sea records the precise timing of early Miocene depositional gaps is not yet resolved and could coincide with the condensed interval in 1168 (Sibert and Rubin, 2021). Age assignments remain less precise in the middle **OligoceneMiocene** (25 to 27 Ma) due to the low rate of change and reversals in $^{87}\text{Sr}/^{86}\text{Sr}$ during this time interval, as well

360 as the current low $^{87}\text{Sr}/^{86}\text{Sr}$ sample coverage.
361

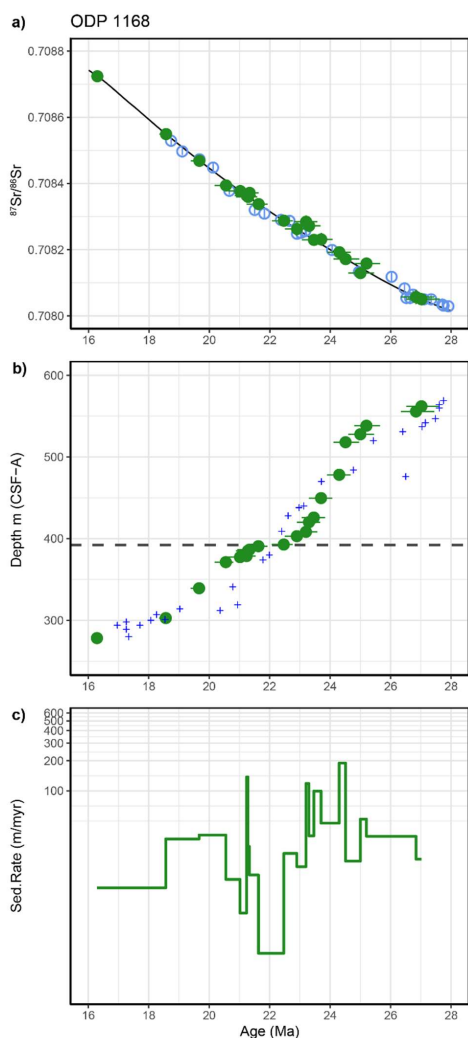


Figure 65: a) Site 1168 $^{87}\text{Sr}/^{86}\text{Sr}$ data (green) vs age (CENOGRID scale) assigned here; also shown are the Site 1218 new data (blue open symbols) and the GTS LOESS curve (Mearthur et al., 2020) b). Age depth plot for Site 1168. Green diamonds denote the ages from $^{87}\text{Sr}/^{86}\text{Sr}$ compared to previous biostratigraphy derived tie points (crosses). c) Sedimentation rate implied by the $^{87}\text{Sr}/^{86}\text{Sr}$ age model. The horizontal dashed line in b) highlights the period of significantly slowed sedimentation of the Early Miocene.

5 Conclusions

The $^{87}\text{Sr}/^{86}\text{Sr}$ record from the astrochronologically dated Site 1218 provides the opportunity to assess ~ 1 m.y. variations in the Sr flux to the ocean during a period of dynamic Antarctic cryosphere evolution. Our dataset resolves relationships between the locus and/or intensity of continental weathering and phases of Antarctic glaciation. Overall, the data suggest that the major changes in mid-Oligocene high latitude climate – particularly the onset and end of the MOGI – do exhibit a close coupling between seawater $^{87}\text{Sr}/^{86}\text{Sr}$ and benthic $\delta^{18}\text{O}$. During periods of expanded ice coverage on Antarctica such as the MOGI, then, our data are consistent with either northward shifts in the ITCZ precipitation to areas of nonradiogenic bedrock, and/or lowered weathering fluxes from highly radiogenic glacial flours on Antarctic. Future, higher resolution sampling is required to further evaluate the significance of such changes. Additionally, the new $^{87}\text{Sr}/^{86}\text{Sr}$ record from sites 1168 and U1406 improve the precision of age

394 correlation of these Northern Hemisphere and Southern Hemisphere mid-latitude sites with each other and with
 395 high resolution benthic $\delta^{18}\text{O}$ records aligned to the CENOGRID chronology.

396 Competing interests

397 The contact author has declared that none of the authors has any competing interests.

398 Acknowledgments

399 This study was supported by the Swiss National Science Foundation (Award 200021_182070 to Heather M. Stoll).

400 We thank Romain Alosius for assistance picking foraminifera, and Laura Arnold for initial evaluation of

401 foraminifera preservation. We gratefully acknowledge the Ocean Drilling Program and International Ocean
402 Discovery Program for providing the samples used in this study.

403 **Author contributions**

404 The study was conceived by HMS. Samples were selected by HMS with advice from HP. Foraminifera were
405 prepared by JG, IHA, and TT. Sr isotope analyses were completed by [LDP](#). Interpretation was completed by
406 HMS and figures were prepared by HMS and [JPG](#). The manuscript was written by HMS with input from all
407 authors.

408

409

410

411 Table 1. ODP identifiers, CENOGRID age, and $^{87}\text{Sr}/^{86}\text{Sr}$ data for Site 1218.

Lab ID	Exp	Site	Hole	Core	Core Type	Section	Section Half	Top Interval (cm)	Bottom Interval (cm)	depth (mcd, m)	age CENOGRID (Ma)	$^{87}\text{Sr}/^{86}\text{Sr}$	Internal SE (2 σ)
B2	199	1218	B	7	H	1	W	125	130	59.93	18.73	0.708529	1.71E-05
B3	199	1218	B	7	H	3	W	75	80	62.43	19.10	0.708497	1.13E-05
A1	199	1218	A	7	H	3	W	50	55	67.29	19.67	0.708473	1.21E-05
A2	199	1218	A	7	H	5	W	50	55	70.29	20.12	0.708448	1.71E-05
B4	199	1218	B	8	H	3	W	100	105	73.29	20.66	0.708378	1.17E-05
B5	199	1218	B	9	H	3	W	32	37	82.07	21.50	0.708320	1.21E-05
B6	199	1218	B	9	H	5	W	105	110	85.45	21.82	0.708309	1.71E-05
A4	199	1218	A	9	H	4	W	82	87	90.32	22.37	0.708290	1.71E-05
A5	199	1218	A	9	H	6	W	20	25	92.67	22.65	0.708287	1.71E-05
B7	199	1218	B	10	H	3	W	82	87	94.54	22.90	0.708248	1.50E-05
B8	199	1218	B	10	H	4	W	87	92	96.12	23.03	0.708251	1.06E-05
B9	199	1218	B	10	H	5	W	141	146	98.17	23.17	0.708256	1.19E-05
B11	199	1218	B	11	H	3	W	147	150	107.26	24.06	0.708199	1.71E-05
B12	199	1218	B	12	H	3	W	107	112	118.18	24.95	0.708133	1.71E-05
B13	199	1218	B	13	H	6	W	17	22	131.57	26.03	0.708118	1.71E-05
1218A 14H1 15-25cm	199	1218	A	14	H	1	W	15	25	138.00	26.46	0.708083	1.82E-05
A9	199	1218	A	14	H	1	W	100	105	138.73	26.52	0.708054	1.71E-05
1218A 14H2 115cm	199	1219	A	15	H	2	W	115	117	140.27	26.64	0.708054	1.84E-05
A10	199	1218	A	14	H	3	W	80	85	141.59	26.74	0.708064	1.71E-05
1218B 15H1 35cm	199	1218	B	15	H	1	W	35	38		27.04	0.708070	1.86E-05
B14	199	1218	B	15	H	2	W	30	35	147.04	27.10	0.708050	1.13E-05
B15	199	1218	B	15	H	4	W	80	85	150.56	27.34	0.708050	1.33E-05
1218B 16H1 25cm	199	1218	B	16	H	1	W	25	26.5	156.17	27.71	0.708034	1.82E-05
B16	199	1218	B	16	H	1	W	70	75	156.63	27.75	0.708031	1.71E-05
B17	199	1218	B	16	H	2	W	107	112	158.55	27.91	0.708029	1.21E-05
B18	199	1218	B	16	H	5	W	60	65	162.03	28.15	0.708031	1.13E-05
C1	199	1218	C	10	H	2	W	100	105	164.77	28.42	0.708023	1.13E-05
1218C 10H3 5cm	199	1218	C	10	H	3	W	5	7	165.25	28.45	0.708019	1.82E-05
B19	199	1218	B	17	H	3	W	120	125	170.40	28.65	0.707982	1.21E-05
1218C 11H1 115cm	199	1218	C	11	H	1	W	115	117	173.77	28.91	0.708003	1.84E-05
C2	199	1218	C	11	H	2	W	130	135	175.45	29.03	0.707986	1.21E-05
B20	199	1218	B	18	H	5	W	10	15	182.15	29.43	0.708006	1.21E-05
A11	199	1218	A	18	H	4	W	37	45	185.68	29.66	0.707988	1.12E-05
A12	199	1218	A	19	H	2	W	67	75	192.20	30.14	0.707976	1.71E-05
1218C 12H6 85cm	199	1218	C	12	X	6	W	85	87	191.63	30.17	0.707974	1.91E-05
B21	199	1218	B	20	X	3	W	117	122	199.97	30.73	0.707956	1.71E-05
B23	199	1218	B	21	X	4	W	12	17	211.94	31.55	0.707930	1.50E-05

412

413

414

415

416

417

418 **Table 2. ⁸⁷Sr/⁸⁶Sr data for Site U1406 and the assigned ages and age uncertainties.**

Site	Hole	Core	Core Type	Section	Section Half	Top Interval (cm)	Bottom Interval (cm)	Depth CCSF-A (m)	Depth CCSF-A (m)	⁸⁷ Sr/ ⁸⁶ Sr	Internal SE (2σ)	midpoint age assigned (Ma)	lower age (Ma)	upper age (Ma)
1406	A	2	H	4	w	89	93	11.61	23.9	0.708625	0.000018	17.60	17.45	17.75
1406	A	2	H	5	w	36	40	12.58	24.9	0.708607	0.000018	17.82	17.67	17.97
1406	A	3	H	2	w	5	8	17.14	25.7	0.708582	0.000004	18.14	17.99	18.29
1406	A	3	H	4	w	89	92	20.98	29.6	0.708556	0.000004	18.43	18.28	18.58
1406	A	3	H	7	w	8	12	24.68	33.3	0.708556	0.000004	18.52	18.30	18.70
1406	A	4	h	1	w	139	143	26.61	34.7	0.708372	0.000004	20.66	20.29	20.91
1406	A	4	H	3	w	81	85	29.03	37.2	0.708350	0.000004	21.00	20.60	21.30
1406	A	5	H	2	w	6	9	36.27	45.4	0.708323	0.000003	21.30	20.90	21.60
1406	A	5	H	4	w	33	37	39.55	48.7	0.708341	0.000004	21.40	21.00	21.70
1406	A	6	H	6	w	74	80	52.47	63.0	0.708303	0.000004	22.20	21.80	22.50
1406	A	8	H	3	w	16	22	66.39	77.6	0.708267	0.000003	22.81	22.41	23.11
1406	C	8	H	1	w	80	84	80.3	80.3	0.708271	0.000014	22.90	22.50	23.20
1406	A	9	H	1	w	62	68	73.35	84.8	0.708252	0.000005	23.03	22.63	23.41
1406	A	9	H	6	w	91	95	81.16	92.6	0.708257	0.000004	23.15	22.75	23.53
1406	B	10	H	3	w	140	144	95.6	95.6	0.708249	0.000013	23.19	22.79	23.57
1406	B	10	H	5	w	70	74	97.9	97.9	0.708238	0.000013	23.32	22.92	23.69
1406	A	10	H	4	w	127	133	88.00	101.8	0.708208	0.000004	23.85	23.45	24.23
1406	A	11	H	3	w	53	59	95.26	109.2	0.708191	0.000004	24.16	23.76	24.54
1406	A	12	H	1	w	90	94	102.12	117.3	0.708161	0.000006	24.72	24.32	25.09
1406	A	12	H	6	w	44	48	109.16	124.4	0.708142	0.000007	25.07	24.67	25.52
1406	A	13	H	7	w	21	25	119.45	135.0	0.708126	0.000004	25.37	24.97	25.82
1406	A	14	H	4	w	97	103	125.70	141.8	0.708112	0.000007	25.64	25.24	26.09
1406	A	15	H	2	w	6	10	131.28	148.7	0.708097	0.000003	25.95	25.55	26.40
1406	A	15	H	5	w	103	107	136.81	154.3	0.708090	0.000004	26.10	25.70	26.55
1406	A	16	H	4	w	26	30	143.98	162.1	0.708074	0.000004	26.37	25.97	26.82
1406	A	16	H	6	w	66	70	147.38	165.5	0.708074	0.000005	26.52	26.12	26.97
1406	A	17	H	1	w	128	132	149.40	170.1	0.708068	0.000005	26.58	26.18	27.03
1406	A	17	H	4	w	86	90	153.48	174.2	0.708039	0.000003	27.31	26.71	28.21
1406	A	17	H	5	w	136	140	155.48	176.2	0.707999	0.000018	28.59	27.99	29.59
1406	A	18	H	1	w	19	23	157.51	184.7	0.707997	0.000018	28.68	28.08	29.68
1406	A	18	H	2	w	94	98	159.60	186.8	0.707984	0.000018	29.24	28.64	30.24
1406	A	18	H	4	w	20	24	161.86	189	0.707982	0.000004	29.33	28.73	30.33
1406	A	18	H	5	w	96	100	164.12	191	0.707976	0.000018	29.58	28.98	30.58
1406	A	19	H	2	w	15	19	166.37	200	0.707966	0.000018	29.97	29.37	30.97

419

420

421

422

423

424 Table 3. ⁸⁷Sr/⁸⁶Sr data for Site 1168 and the assigned ages and age uncertainties.

Site	Hole	Core	Core Type	Section	Section Half	Top Interval (cm)	Bottom Interval (cm)	Depth (mbsf)	⁸⁷ Sr/ ⁸⁶ Sr	Internal SE (2σ)	central age (Ma)	min age (Ma)	max age (Ma)
1168	A	30	X	5	W	2	8	278.25	0.708724	1.82E-05	16.29	16.14	16.44
1168	A	33	X	2	W	52	58	302.75	0.7085492	1.82E-05	18.57	18.35	18.74
1168	A	37	X	1	W	43	49	339.26	0.7084685	1.82E-05	19.67	19.39	19.87
1168	A	40	X	3	W	59.5	64.5	371.22	0.7083942	1.82E-05	20.55	20.18	20.80
1168	A	41	X	1	W	5	7.5	377.36	0.7083771	1.41E-05	21.02	20.62	21.32
1168	A	41	X	1	W	135	138	378.66	0.7083633	1.35E-05	21.24	20.84	21.54
1168	A	41	X	6	W	34	36.5	385.15	0.7083596	1.35E-05	21.28	20.88	21.58
1168	A	41	X	7	W	34	47.5	386.46	0.7083715	1.41E-05	21.33	20.93	21.63
1168	A	42	X	3	W	45	25.5	390.78	0.7083377	1.62E-05	21.63	21.23	21.93
1168	A	42	X	4	W	137	139	392.78	0.7082875	1.76E-05	22.47	22.07	22.77
1168	A	43	X	5	W	55	57	403.06	0.7082624	1.95E-05	22.90	22.50	23.28
1168	A	44	X	2	W	69	71	408.3	0.7082843	1.95E-05	23.20	22.80	23.58
1168	A	45	X	3	W	143	145	420.14	0.708272	1.92E-05	23.30	22.90	23.68
1168	A	46	X	1	W	49	55	425.82	0.7082296	1.82E-05	23.46	23.06	23.84
1168	A	48	X	4	W	65	67.5	449.65	0.708231	1.95E-05	23.70	23.30	24.08
1168	A	51	X	4	W	38	42	478.2	0.7081923	1.82E-05	24.30	23.90	24.68
1168	A	55	X	5	W	33	39	518.06	0.7081716	1.82E-05	24.51	24.11	24.96
1168	A	56	X	5	W	37	43	527.8	0.7081292	1.82E-05	25.00	24.60	25.45
1168	A	57	X	5	W	113	117	538.25	0.7081581	1.86E-05	25.20	24.80	25.65
1168	A	59	X	4	W	83	87	555.75	0.7080568	2.19E-05	26.84	26.34	27.44
1168	A	60	X	2	W	57	61	562.09	0.7080503	1.84E-05	27.02	26.52	27.62

Formatted: Normal

425

Site	Hole	Core	Core Type	Section	Section Half	Top Interval (cm)	Bottom Interval (cm)	Depth CSF-A (m)	$^{87}\text{Sr}/^{86}\text{Sr}$	Internal St (2- σ)	Central age (Ma)	Min age (Ma)	Max age (Ma)
1168	A	30	X	5	W	2	8	278.25	0.708724	1.82E-05	16.29	16.14	16.44
1168	A	33	X	2	W	52	58	302.75	0.7085492	1.82E-05	18.57	18.35	18.74
1168	A	37	X	1	W	43	49	339.26	0.7084685	1.82E-05	19.67	19.39	19.87
1168	A	40	X	3	W	59.5	64.5	371.22	0.7083942	1.82E-05	20.55	20.18	20.80
1168	A	41	X	1	W	5	7.5	377.36	0.7083771	1.41E-05	21.02	20.62	21.32
1168	A	41	X	1	W	135	138	378.66	0.7083633	1.35E-05	21.24	20.84	21.54
1168	A	41	X	6	W	34	36.5	385.15	0.7083596	1.35E-05	21.28	20.88	21.58
1168	A	41	X	7	W	34	47.5	386.46	0.7083715	1.41E-05	21.33	20.93	21.63
1168	A	42	X	3	W	45	25.5	390.78	0.7083377	1.62E-05	21.63	21.23	21.93
1168	A	42	X	4	W	137	139	392.78	0.7082875	1.76E-05	22.47	22.07	22.77
1168	A	43	X	5	W	55	57	403.06	0.7082624	1.95E-05	22.90	22.50	23.28
1168	A	44	X	2	W	69	71	408.3	0.7082843	1.95E-05	23.20	22.80	23.58
1168	A	45	X	3	W	143	145	420.14	0.708272	1.92E-05	23.30	22.90	23.68
1168	A	46	X	1	W	49	55	425.82	0.7082296	1.82E-05	23.46	23.06	23.84
1168	A	48	X	4	W	65	67.5	449.65	0.708231	1.95E-05	23.70	23.30	24.08
1168	A	51	X	4	W	38	42	478.2	0.7081923	1.82E-05	24.30	23.90	24.68
1168	A	55	X	5	W	33	39	518.06	0.7081716	1.82E-05	24.51	24.11	24.96
1168	A	56	X	5	W	37	43	527.8	0.7081292	1.82E-05	25.00	24.60	25.45
1168	A	57	X	5	W	113	117	538.25	0.7081581	1.86E-05	25.20	24.80	25.65
1168	A	59	X	4	W	83	87	555.75	0.7080568	2.19E-05	26.84	26.34	27.44
1168	A	60	X	2	W	57	61	562.09	0.7080503	1.84E-05	27.02	26.52	27.62

426

427

428

429

430

431

432 **References**

433

434

435

- 436 Atwood, A. R., Donohoe, A., Battisti, D. S., Liu, X., and Pausata, F. S.: Robust longitudinally variable responses of the ITCZ
437 to a myriad of climate forcings, *Geophysical Research Letters*, 47, e2020GL088833, doi.org/10.1029/2020GL088833, 2020.
- 438 Boyle, P. R., Romans, B. W., Tucholke, B. E., Norris, R. D., Swift, S. A., and Sexton, P. F.: Cenozoic North Atlantic deep
439 circulation history recorded in contourite drifts, offshore Newfoundland, Canada, *Marine Geology*, 385, 185-203,
440 doi.org/10.1016/j.margeo.2016.12.014, 2017.
- 441 Cande, S. C. and Kent, D. V.: A new geomagnetic polarity time scale for the Late Cretaceous and Cenozoic, *Journal of*
442 *Geophysical Research: Solid Earth*, 97, 13917-13951, doi.org/10.1029/92JB01202, 1992.
- 443 De Vleeschouwer, D., Vahlenkamp, M., Crucifix, M., and Pälike, H.: Alternating Southern and Northern Hemisphere climate
444 response to astronomical forcing during the past 35 my, *Geology*, 45, 375-378, doi.org/10.1130/G38663.1, 2017.
- 445 Egger, L. M., Bahr, A., Friedrich, O., Wilson, P. A., Norris, R. D., van Peer, T. E., Lippert, P. C., Liebrand, D., and Pross, J.:
446 Sea-level and surface-water change in the western North Atlantic across the Oligocene–Miocene Transition: a palynological
447 perspective from IODP Site U1406 (Newfoundland margin), *Marine Micropaleontology*, 139, 57-71,
448 doi.org/10.1016/j.marmicro.2017.11.003, 2018.
- 449 Exon, N. F., Kennett, J. P., and Malone, M. J.: Leg 189 synthesis: Cretaceous–Holocene history of the Tasmanian gateway,
450 *Proceedings of the ocean drilling program, scientific results*, 1-37, doi:10.2973/odp.proc.sr.189.101.2004.
- 451 Farmer, G. L., Barber, D., and Andrews, J.: Provenance of Late Quaternary ice-proximal sediments in the North Atlantic: Nd,
452 Sr and Pb isotopic evidence, *Earth and Planetary Science Letters*, 209, 227-243, doi.org/10.1016/S0012-821X(03)00068-2,
453 2003.
- 454 Farmer, G. L., Licht, K., Swope, R. J., and Andrews, J.: Isotopic constraints on the provenance of fine-grained sediment in
455 LGM tills from the Ross Embayment, Antarctica, *Earth and Planetary Science Letters*, 249, 90-107,
456 doi.org/10.1016/j.epsl.2006.06.044, 2006.
- 457 Galy, A., France-Lanord, C., and Derry, L. A.: The Late Oligocene–Early Miocene Himalayan belt constraints deduced from
458 isotopic compositions of Early Miocene turbidites in the Bengal Fan, *Tectonophysics*, 260, 109-118, 1996.
- 459 Guitián, J. and Stoll, H. M.: Evolution of Sea Surface Temperature in the Southern Mid-latitudes from Late Oligocene through
460 Early Miocene, *Paleoceanography and Paleoclimatology*, 36, e2020PA004199, doi.org/10.1029/2020PA004199, 2021.
- 461 Hodell, D. A., Mead, G. A., and Mueller, P. A.: Variation in the strontium isotopic composition of seawater (8 Ma to present):
462 Implications for chemical weathering rates and dissolved fluxes to the oceans, *Chemical Geology: Isotope Geoscience section*,
463 80, 291-307, 1990.
- 464 Hoem, F. S., Sauermilch, I., Hou, S., Brinkhuis, H., Sangiorgi, F., and Bijl, P. K.: Late Eocene–early Miocene evolution of
465 the southern Australian subtropical front: a marine palynological approach, *Journal of*
466 *Micropaleontology*, 40, 175-193, doi.org/10.5194/jm-40-175-2021, 2021, 2021.
- 467 Hoem, F. S., Sauermilch, I., Aleksinski, A. K., Huber, M., Peterse, F., Sangiorgi, F., and Bijl, P. K.: Strength and variability
468 of the Oligocene Southern Ocean surface temperature gradient, *Communications Earth & Environment*, 3, 322,
469 doi.org/10.1038/s43247-022-00666-5, 2022.
- 470 Holbourn, A., Kuhnt, W., Kochhann, K. G., Andersen, N., and Sebastian Meier, K.: Global perturbation of the carbon cycle
471 at the onset of the Miocene Climatic Optimum, *Geology*, 43, 123-126, doi.org/10.1130/G36317.1, 2015.
- 472 Jamieson, S. S., Sugden, D. E., and Hulton, N. R.: The evolution of the subglacial landscape of Antarctica, *Earth and Planetary*
473 *Science Letters*, 293, 1-27, doi.org/10.1016/j.epsl.2010.02.012, 2010.
- 474 Kent, D. V. and Muttoni, G.: Modulation of Late Cretaceous and Cenozoic climate by variable drawdown of atmospheric pCO
475 2 from weathering of basaltic provinces on continents drifting through the equatorial humid belt, *Climate of the Past*, 9, 525-
476 546, doi.org/10.5194/cp-9-525-2013, 2013.
- 477 Kim, B. and Zhang, Y. G.: Methane hydrate dissociation across the Oligocene–Miocene boundary, *Nature Geoscience*, 15,
478 203-209, doi.org/10.1038/s41561-022-00895-5, 2022.
- 479 Kirkham, R., Chorlton, L., and Carriere, J.: Generalized geology of the world, Generalized geological map of the world and
480 linked databases. Geological Survey of Canada, Open File 2915d, 1995.
- 481 Krishnaswami, S., Trivedi, J., Sarin, M., Ramesh, R., and Sharma, K.: Strontium isotopes and rubidium in the Ganga-
482 Brahmaputra river system: Weathering in the Himalaya, fluxes to the Bay of Bengal and contributions to the evolution of
483 oceanic ⁸⁷Sr/⁸⁶Sr, *Earth and Planetary Science Letters*, 109, 243-253, doi.org/10.1016/0012-821X(92)90087-C, 1992.
- 484 Licht, K. J. and Hemming, S. R.: Analysis of Antarctic glacial sediment provenance through geochemical and petrologic
485 applications, *Quaternary Science Reviews*, 164, 1-24, doi.org/10.1016/j.quascirev.2017.03.009, 2017.
- 486 Liebrand, D., Beddow, H. M., Lourens, L. J., Pälike, H., Raffi, I., Bohaty, S. M., Hilgen, F. J., Saes, M. J., Wilson, P. A., and
487 van Dijk, A. E.: Cyclostratigraphy and eccentricity tuning of the early Oligocene through early Miocene (30.1–17.1 Ma):
488 *Cibicides mundulus* stable oxygen and carbon isotope records from Walvis Ridge Site 1264, *Earth and Planetary Science*
489 *Letters*, 450, 392-405, doi.org/10.1016/j.epsl.2016.06.007, 2016.
- 490 Liebrand, D., de Bakker, A. T., Beddow, H. M., Wilson, P. A., Bohaty, S. M., Ruessink, G., Pälike, H., Batenburg, S. J.,
491 Hilgen, F. J., and Hodell, D. A.: Evolution of the early Antarctic ice ages, *Proceedings of the National Academy of Sciences*,
492 114, 3867-3872, 2017.
- 493 Liu, Z., He, Y., Jiang, Y., Wang, H., Liu, W., Bohaty, S. M., and Wilson, P. A.: Transient temperature asymmetry between
494 hemispheres in the Palaeogene Atlantic Ocean, *Nature Geoscience*, 11, 656-660, doi.org/10.1038/s41561-018-0182-9, 2018.

495 McArthur, J., Howarth, R., Shields, G., and Zhou, Y.: Strontium isotope stratigraphy, in: *Geologic time scale 2020*, Elsevier,
496 211-238, doi.org/10.1016/B978-0-12-824360-2.00007-3, 2020.

497 Mead, G. A. and Hodell, D. A.: Controls on the $87\text{Sr}/86\text{Sr}$ composition of seawater from the middle Eocene to Oligocene:
498 Hole 689B, Maud Rise, Antarctica, *Paleoceanography*, 10, 327-346, doi.org/10.1029/94PA03069, 1995.

499 Miller, K. G., Feigenson, M. D., Kent, D. V., and Olsson, R. K.: Upper Eocene to Oligocene isotope ($87\text{Sr}/86\text{Sr}$, $\delta^{18}\text{O}$, $\delta^{13}\text{C}$)
500 standard section, Deep sea drilling Project site 522, *Paleoceanography*, 3, 223-233, doi.org/10.1029/PA003i002p00223, 1988.

501 Miller, K. G., Feigenson, M. D., Wright, J. D., and Clement, B. M.: Miocene isotope reference section, Deep Sea Drilling
502 Project Site 608: an evaluation of isotope and biostratigraphic resolution, *Paleoceanography*, 6, 33-52,
503 doi.org/10.1029/90PA01941, 1991.

504 Myrow, P. M., Hughes, N. C., Derry, L. A., McKenzie, N. R., Jiang, G., Webb, A. A. G., Banerjee, D. M., Paulsen, T. S., and
505 Singh, B. P.: Neogene marine isotopic evolution and the erosion of Lesser Himalayan strata: Implications for Cenozoic tectonic
506 history, *Earth and Planetary Science Letters*, 417, 142-150, 2015.

507 Norris, R., Wilson, P., and Blum, P.: Proceedings of the Integrated Ocean Drilling Program Exp. 342, College Station, TX:
508 Integrated Ocean Drilling Program, doi.org/10.2204/iodp.proc.342.107.2014, 2014.

509 Oslick, J. S., Miller, K. G., Feigenson, M. D., and Wright, J. D.: Oligocene-Miocene strontium isotopes: Stratigraphic revisions
510 and correlations to an inferred glacioeustatic record, *Paleoceanography*, 9, 427-443, doi.org/10.1029/94PA00249, 1994.

511 Pälike, H., Norris, R. D., Herrle, J. O., Wilson, P. A., Coxall, H. K., Lear, C. H., Shackleton, N. J., Tripathi, A. K., and Wade,
512 B. S.: The heartbeat of the Oligocene climate system, *science*, 314, 1894-1898, DOI: 10.1126/science.1133822, 2006.

513 Palmer, M. and Elderfield, H.: Sr isotope composition of sea water over the past 75 Myr, *Nature*, 314, 526-528,
514 doi.org/10.1038/314526a0, 1985.

515 Paytan, A., Griffith, E. M., Eisenhauer, A., Hain, M. P., Wallmann, K., and Ridgwell, A.: A 35-million-year record of seawater
516 stable Sr isotopes reveals a fluctuating global carbon cycle, *Science*, 371, 1346-1350, 2021.

517 Pena, L., Calvo, E., Cacho, I., Eggins, S., and Pelejero, C.: Identification and removal of Mn-Mg-rich contaminant phases on
518 foraminiferal tests: Implications for Mg/Ca past temperature reconstructions, *Geochemistry, Geophysics, Geosystems*, 6,
519 doi.org/10.1029/2005GC000930, 2005.

520 Peucker-Ehrenbrink, B. and Fiske, G. J.: A continental perspective of the seawater $87\text{Sr}/86\text{Sr}$ record: a review, *Chemical*
521 *Geology*, 510, 140-165, /doi.org/10.1016/j.chemgeo.2019.01.017, 2019.

522 Raymo, M. E., Ruddiman, W. F., and Froelich, P. N.: Influence of late Cenozoic mountain building on ocean geochemical
523 cycles, *Geology*, 16, 649-653, doi.org/10.1130/0091-7613(1988)016<0649:IOLCMB>2.3.CO;2, 1988.

524 Reilly, T. J., Miller, K. G., and Feigenson, M. D.: Latest Eocene-earliest Miocene Sr isotopic reference section, Site 522,
525 eastern South Atlantic, *Paleoceanography*, 17, 18-11-18-19, doi.org/10.1029/2001PA000745, 2002.

526 Scher, H. D., Whittaker, J. M., Williams, S. E., Latimer, J. C., Kordesch, W. E., and Delaney, M. L.: Onset of Antarctic
527 Circumpolar Current 30 million years ago as Tasmanian Gateway aligned with westerlies, *Nature*, 523, 580-583,
528 doi.org/10.1038/nature14598, 2015.

529 Sibert, E. C. and Rubin, L. D.: An early Miocene extinction in pelagic sharks, *Science*, 372, 1105-1107, DOI:
530 10.1126/science.aaz3549, 2021.

531 Spray, J. F., Bohaty, S. M., Davies, A., Bailey, I., Romans, B. W., Cooper, M. J., Milton, J. A., and Wilson, P. A.: North
532 Atlantic evidence for a unipolar icehouse climate state at the Eocene-Oligocene Transition, *Paleoceanography and*
533 *Paleoclimatology*, 34, 1124-1138, doi.org/10.1029/2019PA003563, 2019.

534 Stickle, C., Brinkhuis, H., McGonigal, K., Chaproniere, G., Fuller, M., Kelly, D., Nürnberg, D., Pfuhl, H., Schellenberg, S.,
535 and Schönfeld, J.: Late Cretaceous–Quaternary biomagnetostratigraphy of ODP Sites 1168, 1170, 1171, and 1172, Tasmanian
536 Gateway, Proceedings of the Ocean Drilling Program, Scientific Results, 1-57, doi:10.2973/odp.proc.sr.189.111.2004,
537 van Peer, T. E., Xuan, C., Lippert, P. C., Liebrand, D., Agnini, C., and Wilson, P. A.: Extracting a detailed magnetostratigraphy
538 from weakly magnetized, Oligocene to early Miocene sediment drifts recovered at IODP Site U1406 (Newfoundland margin,
539 northwest Atlantic Ocean), *Geochemistry, Geophysics, Geosystems*, 18, 3910-3928, doi.org/10.1002/2017GC007185, 2017a.

540 van Peer, T. E., Liebrand, D., Xuan, C., Lippert, P. C., Agnini, C., Blum, N., Blum, P., Bohaty, S. M., Bown, P., and Greenop,
541 R.: Data report: revised composite depth scale and splice for IODP Site U1406, doi:10.2204/iodp.proc.342.202.2017, 2017b.

542 Westerhold, T., Marwan, N., Drury, A. J., Liebrand, D., Agnini, C., Anagnostou, E., Barnett, J. S., Bohaty, S. M., De
543 Vleeschouwer, D., and Florindo, F.: An astronomically dated record of Earth's climate and its predictability over the last 66
544 million years, *Science*, 369, 1383-1387, DOI: 10.1126/science.aba685, 2020.

545 Yang, Y., Galy, A., Yang, R., Liu, Y., Zhang, W., Ruan, X., Fang, X., Jin, Z., Song, B., and Yan, M.: Intense metamorphism-
546 generated radiogenic Sr regulated Cenozoic water Sr isotope evolution on the NE Tibetan Plateau: A perspective on Qilian
547 orogen denudation and Asian eolian transport, *Geological Society of America Bulletin*, 2022.

548 Zachos, J. C., Opdyke, B. N., Quinn, T. M., Jones, C. E., and Halliday, A. N.: Early Cenozoic glaciation, Antarctic weathering,
549 and seawater $87\text{Sr}/86\text{Sr}$: Is there a link?, *Chemical Geology*, 161, 165-180, doi.org/10.1016/S0009-2541(99)00085-6, 1999.

551